A combined experimental and computational study of phase-change dynamics and flow inside a sessile water droplet freezing due to interfacial heat transfer

Victor Voulgaropoulos[a], Mohammadreza Kadivar[b], Mohammad Moghimi Ardekani[c], Mohamed Maher[a], Hameed Alawadi[a,d], Omar K. Matar[a], Christos N. Markides[a,e,*]

[a] *Department of Chemical Engineering, Imperial College London, South Kensington Campus, London SW7 2AZ, UK*
[b] *Department of Mechanical and Manufacturing Engineering, Institute of Technology Sligo, Sligo, Ireland*
[c] *Department of Engineering, Staffordshire University, Stoke-On-Trent ST4 2DE, UK*
[d] *Department of Mechanical Power and Refrigeration Technology, College of Technological Studies, Kuwait*
[e] *Kutateladze Institute of Thermophysics, Novosibirsk, Russian Federation*

* Corresponding author: *Email address:* c.markides@imperial.ac.uk (Christos N. Markides)

N.B.: This is the ACCEPTED version of this article. The final, published version of the article can be found at: https://doi.org/10.1016/j.ijheatmasstransfer.2021.121803

Abstract

This study experimentally and numerically investigates the freezing characteristics and fluid dynamics of millimetre-sized sessile water droplets submerged in silicone oil at sub-zero temperatures under free convection. Individual water droplets were cooled to sub-zero temperatures (260-270 K) via interfacial heat transfer between the two liquid phases, in an approach different to studies in the literature where the cooling is done either from the solid substrate or from a low-temperature gas phase (such as air) surrounding the droplets. Laser-induced fluorescence was employed to perform spatiotemporally-resolved measurements of the phase distribution (from which interface distributions, freezing fronts, and rates were extracted). The particle image velocimetry was used to generate information on the velocity fields inside the liquid droplets. The experimental data are complemented by computational fluid dynamics (CFD) simulations, which showed acceptable qualitative and quantitative agreement with the experimental results. The experimental and simulation results indicated that prior to the initiation of freezing, two counteracting recirculation zones are generated in the central plane of the droplets, one on either side of the centreline, leading to a net upward flow at the edges and a downward flow in the centre due to the natural convection driven by internal temperature gradients. The nucleation sites appear on the external regions of the recirculation structures (which are locations with higher shear). Once freezing starts, the natural circulation patterns are suppressed, and instead, a sole downwards flow dominates, which is the result of the freezing layer suppressing the water phase. CFD results demonstrated a relatively wide temperature and pressure distribution in the water droplet at the beginning of the freezing stage, which gradually diminishes as the freezing process proceeds. The effect of droplet size and oil temperature on the freezing rates were investigated parametrically. The finding showed that when the droplet size doubles, the time required for the droplet to completely freeze extended by almost an order of magnitude. In addition, lower oil temperatures appeared to modify the normalised freezing rate, with sharper exponential growth rates and reduced initial and final stages at higher oil temperatures.

Keywords: CFD, LIF, PIV, droplets, emulsion, freezing, laser diagnostics, liquid-liquid, solidification

1. Introduction

Freezing is a ubiquitous phenomenon both in nature and in engineering applications. It is encountered in a wide range of industrial systems such as wind turbines [1], thermal energy storage systems [2], heat exchangers [3], food storage [4], and groundwater freezing [5]. Freezing possesses are inherently complex, as they involve a plethora of heat and mass transfer, fluid mechanical, and thermodynamic interacting phenomena that span multiple time and length scales, which, apart from the interest of the industrial community, also stimulate investigations of fundamental nature.

The characteristics of transient temperature changes during the process of droplet freezing has been described in the literature [4,6–9], as shown in Figure 1(a). The freezing process of pure water comprises five distinctive stages, as illustrated in Figure 1(a): (1) supercooling, (2) nucleation, (3) recalescence, (4) freezing, and (5) solid cooling. In the supercooling stage, the temperature of the drops declines through natural convection heat transfer in the water. If the water contains seed crystals, or 'nuclei', the supercooling stage is halted by the formation of nucleation sites as the temperature reaches the freezing point, T_F. Otherwise, supercooling proceeds, and the temperature of water drops below T_F until nucleation sites form. Nucleation is the starting point of recalescence, which takes place spontaneously over tens of milliseconds during which the temperature quickly reverts to the freezing temperature by releasing latent heat due to rapid kinetic crystal growths from crystal nuclei. At the end of the recalescence, the water droplet becomes a uniform mixture of water and ice with a temperature equal to T_F.

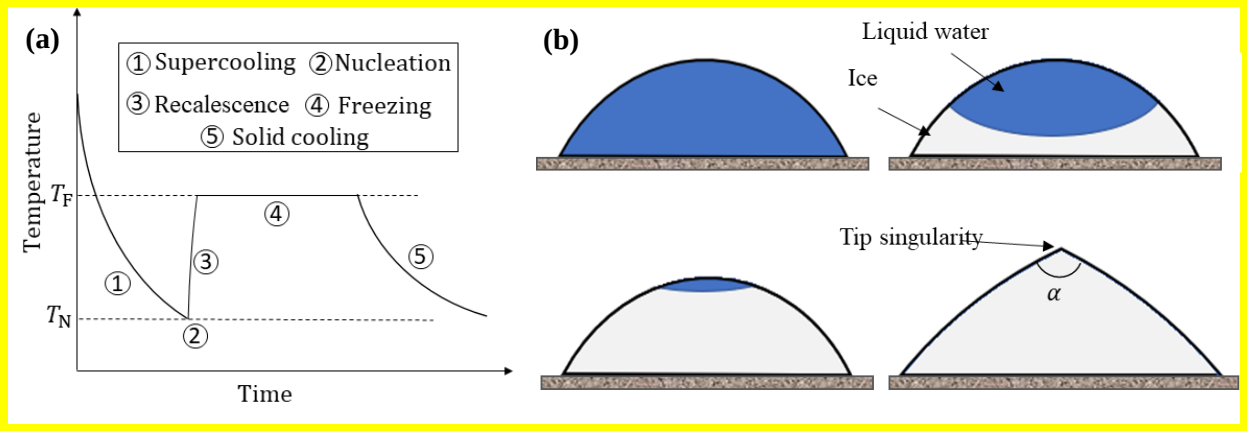

Figure 1. Schematics of: (a) the physical processes and associated temperature transitions, and (b) the shape of the advancing freezing front sessile droplet sitting on a cold surface.

The freezing stage is a longer process compared to the previous stages, during which the water-ice mixture is entirely solidified. The last stage corresponds to solid cooling, during which the temperature decreases by conduction heat transfer in the solidified droplet.

The final shape of the droplet can vary depending on the advancement of the freezing front and boundary conditions. The formation of a conical tip at the final stage of freezing of a sessile water droplet on a cold plate has been reported by several researchers, including Mar ń et al. [10], Duy and Vu [11], and Vu et al. [12], Ismail & Waghmare [13]. When water is being cooled down from a cold plate, the freezing front moves upward as its solidification initiates from the bottom side (the cold plate where the droplet sits on) and moves toward the top of the droplet. Owing to the liquid-vapour surface tension, the unfrozen part of the water droplet remains spherical during the process [14]. However, the frozen part (the formed ice) expands vertically (the expansion does not occur in the radial direction) and pushes against the spherical surface of the liquid [10]. The vertical expansion of the ice and the restricting effect of surface tension leads to a singular shape with a sharp pointy tip [15] (Figure 1(b)).

Many researchers have studied freezing in single and two-fluid systems to predict the conditions which may hinder or optimise the performance of industrial systems. Hindmarsh et al. [6] observed the stages of temperature transition of freezing droplets in a series of experiments, and predicted the freezing times with reasonable accuracy using numerical models. Their work provides an insight into the heat transfer during the freezing process, and other works were later presented using both intrusive and non-intrusive methods [8,16], and including recent work by Yao et al. [17]. Strub et al. [7] performed numerical and experimental studies of the crystallisation of water droplets in humid cold airflows, aimed at understanding the underlying behaviour associated with the freezing water droplets from a snow gun.

Fewer studies have been performed to directly understand the freezing in liquid-liquid systems. Observations have been reported on the hydrate growth at the liquid-liquid interface. In this regard, Sakaguchi et al. [18] observed the crystal morphology of hydrate at the liquid-liquid interface, and Cha et al. [19] looked at ways to prevent hydrate formation at the water-oil interface by employing a hydrophobic silica nanoparticle. Further experimental studies have been carried out to study the freezing of micrometre-sized water droplets and report key parameters affecting the freezing front propagation, i.e., dynamics of the phase transition. These studies utilised two main methods: an intrusive method (e.g., thin mesh or plate) and a non-intrusive one (e.g., free flight or levitation), with the former offering an inexpensive and robust method to accurately measure the temperature transition of a droplet. Temperature evolution on different surfaces was presented by Chaudhary and Li [8], where the numerical temperatures showed good agreement with the experimental data. Jung et al. [20] suggested that environmental conditions can alter the ice crystallisation mechanism, which can significantly influence the pinning of the droplet on a superhydrophobic surface. The topic of water droplets freezing on a substrate has been discussed by a significant number of authors in the literature. An extensive summary of the related literature was compiled by Song et al. [21].

Several studies have used high-speed cameras to visualise the freezing of a sessile water droplet on a cold substrate and presented their results in terms of freezing rates at different initial conditions [14,22,23]. The shape of the droplet after freezing was also a point of interest in some studies [10,24], where the researchers investigated the underlying conditions that can lead to the presence of the singularity tip during the last stages of freezing. Zhang et al. [25,26] presented the effect of hydrophobic and hydrophilic surfaces on the nucleation characteristics and the freezing time, and similar work is presented in Liu et al. [27] for anti-icing surfaces. Hao et al. [28] studied the freezing delay time and freezing time of a stationary droplet on surfaces with various roughness and wettability. They found that surface roughness plays an important role in nucleation. In order to study the impact of surface wettability on freezing processes, Chaudhary and Li [8] investigated surfaces with different wettability subjected to rapid cooling. The study revealed that the freezing time is dependent on the droplet temperature at the pre-recalescence time and the surface wettability. Further work presented in [29] considered different thermal conductivity and similar wettability of three surfaces and visualised the frost formation using high-speed visualisation with direct photography.

In addition, to the above-mentioned experimental studies, a significant number of studies was devoted to a theoretical treatment of a freezing water droplet (e.g., see Ref. [30–34]), or the numerical simulation of solidifying droplets; these included the use of finite element-based [35], volume-of-fluid [36], boundary integral [37,38], front-tracking [39–42], and enthalpy-based methods [8,43]. Hindmarsh et al. [4,6] demonstrated that the assumption of uniform temperature distribution in the droplet is adequately accurate for the droplet sizes under consideration. Based on this assumption, they simplified and solved the transient temperature equation by balancing the internal energy with the dissipated energy from the droplet surface. However, Chaudhary and Li [8] recorded different measured temperature in a freezing droplet. They also solved an enthalpy-based heat conduction equation for the freezing process of droplets subjected to rapid cooling. Zhang et al. [44] assumed that the Stefan problem governs the solidification of liquid, including a moving solid-liquid interface with releasing latent heat. They solved the heat conduction equation of the Stefan problem numerically using equivalent heat capacity, thermal conductivity, and density.

Vu et al. [41] proposed a front-tracking/finite difference method for modelling the solidification of droplets. This method has been validated against several similar problems, including droplet freezing on a cold plate [41,45], solidification around circular cylinders [46,47], and a three-phase solidification process [48]. Vu [39,49,50] employed an interpolation technique in the axisymmetric front-tracking method to enforce the no-slip velocity boundary at the solid-fluid interface. This method was used for the solidification of droplets under forced convection heat transfer. Duy and Vu [11] used a two-dimensional front-tracking method for simulating the solidification of liquid droplets on a vertical wall. They showed that the formation of a conical

tip at the top of a solidified droplet is due to the volume expansion. Similar results were recently reported by Vu et al. [12] for the solidification of a liquid droplet on an inclined surface using the front-tracking method.

Bennon and Incropera [51,52] introduced an enthalpy-based fix grid volume averaging method for solid-liquid phase change systems. This method permits employing the energy equation with the temperature being the primary dependent variable. Based on the fixed grid volume averaging method, Voller et al. [53] and Brent et al. [54] suggested an enthalpy-porosity approach for solving convection-diffusion problems involving solid-liquid phase-change processes. Enthalpy porosity methods have been used and validated for a wide range of problems involving melting and solidification processes [55]. The previously mentioned enthalpy-based methods (i.e., Refs. [8,43]) solve the heat conduction equation (diffusion problem) while ignoring the convection heat transfer. Enthalpy-porosity methods enable the simultaneous solution of convection-diffusion heat transfer in a fixed grid framework. Karlsson et al. [56,57] investigated the influence of the natural convection on the freezing process of water droplet sitting on a cold surface using the enthalpy-porosity approach. They assumed that the droplet volume would not change during the freezing and ignored the supercooling process, and showed that the evolution of the freezing front depends on the internal temperature and the velocity field. Moreover, the average velocity declines with the reduction of cold plate temperature.

In previous studies [6,7,8,10,14,16–29], heat removal was achieved via a cold plate or a cold compressible gas phase. As a complement to those investigations and to identify any differences in the phase-change process, the present study turned to a liquid-liquid system and explored how droplet freezing takes place when the heat removal is brought about by a surrounding incompressible silicone oil at sub-zero temperatures. Laser-based diagnostics were employed to allow for qualitative observations. Moreover, temporally and spatially resolved measurements of phase-field (freezing rate) were accomplished via laser-induced fluorescence (LIF). The velocity field inside a two-dimensional ‘slice’ along the centreline of the droplet was obtained simultaneously via particle image velocimetry (PIV). This study aims to: (i) map the effect of the droplet size and oil temperature on the freezing rates; and (ii) link the flow characteristics to the nucleation mechanism, freezing front propagation and interfacial heat transfer. Apart from the experimental study, computational fluid dynamics (CFD) simulations based on the enthalpy-porosity method were also used to simulate the convection-diffusion heat transfer during the freezing of sessile water droplets surrounded by the oil. The findings were complemented by comparisons with literature data and CFD simulations.

2. Experimental methods

2.1. Apparatus

The schematic of the experimental facility is shown in Figure 2. A glass cuvette open to the ambient air and filled with silicone oil is used to conduct the experiments. The silicone oil is a Dow Corning 200 Fluid with a viscosity of 28 mPa s and a density of 980 kg/m^3 at room temperature and pressure. Heat is removed from the silicone oil using an air-cooled chiller that transports a water-ethylene glycol mixture at sub-zero temperatures to a cooling coil submerged in the glass cuvette. The glass cuvette is a square box with an open top, with side lengths of 10 cm, which is filled close to the top. Considering the volume of the glass cuvette, the amount of oil used is approximately 8 mL. The temperature of the oil is monitored using two K-type thermocouples placed at locations distributed over the inside volume of the cuvette to ensure temperature homogeneity at the start of each trial. The temperature does not vary by more than $\pm$ 0.5 K during any run. The arithmetic mean of the time-averaged values of the thermocouples is used as the nominal oil temperature. A water droplet is injected using a NE-1000 Programmable Single Syringe Pump and needle. The volume of drops in the experiments varies approximately in the range from 1 μL to 30 μL. Droplet deposition was performed by creating a small liquid water droplet close to the bottom of the cuvette (~1 mm from the bottom), and letting this free fall under the action of gravity until it touched the bottom of the cuvette. During this process, i.e., when initialising all experiments, there was no ice present in the cuvette, so the only two substances present were oil and the water droplets. This process took less than 2 s.

The pump employed in this work can be set to operate at flow rates down to 1 μL/hr, which leads to an uncertainty of the droplet volume measurement that is considered negligible (<0.1%). A separate set of tests aimed at quantifying the repeatability of the present experiments was performed at ambient temperature with the cuvette resting on a microscale. By measuring the weight change of the droplets generated by the pump and testing multiple droplets, a deviation below 5% in the weight of the droplets was observed, even for the smallest drops investigated in this work (1 μL). In addition, the temperature measurement uncertainty was less than 0.5 ℃ over the range of tested temperatures.

The oil was cooled down to a set temperature before a water droplet was inserted inside the cuvette, with uniformity ensured by comparing the values of thermocouples placed strategically in the cuvette. The droplet can be assumed to be at near-ambient temperature at the beginning of each experiment. Two slits are cut into the insulation of the cuvette to allow optical access to the high-speed camera and laser, as shown in Figure 2.

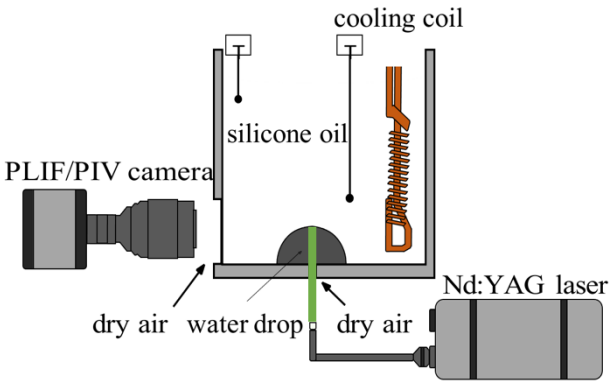

Figure 2. Schematic of the experimental apparatus used for performing the freezing experiments of the millimetre-sized water droplets immersed in silicone oil. Laser sheet is indicated by the green line entering the cuvette from below.

A frequency-doubled Nd:YAG laser (emitting at 532 nm) and dedicated sheet optics are used to generate a 1 mm thin laser-sheet, as shown in Figure 2, are directed perpendicularly towards the bottom of the cuvette. The useful signal emitted from the dye-doped droplet is collected by a VC-Imager Pro HS 500 camera equipped with a 105 mm f/2.8 lens and a 540 nm long-pass filter that is set up at 90◦ to the excitation plane.

2.2. Laser-based measurements

Conventional PIV and LIF measurements are performed using a fluorescent dye (Rhodamine B) and fluorescent tracers (Rhodamine 6G-coated PMMA particles with nominal diameter ~ 10 μm), respectively. The liquid and particle additives are introduced at low concentrations, i.e., below 0.05 ppm, and are mixed thoroughly within the aqueous phase to ensure homogeneity and avoid any concentration gradients. The final magnification of the collection optics is 8.4 μm/pixel.

For the PIV measurements, a sliding mean is first subtracted from the images to isolate the tracer particle signal and improve the particle signal-to-background ratio. DaVis 8.4 (LaVision) software is used to obtain the vector field, performed using a two-pass iterative method, from 64 × 64 pixels to 32 × 32 pixels with a 50% overlap. Any correlation and tracing errors can be neglected. The velocity measurement uncertainties are calculated based on the method by Sciacchitano et al. [58] and using DaVis 10.0 (LaVision) for typical instantaneous velocity fields before and after freezing takes place. The uncertainty of both velocity components does not exceed 5% inside the liquid droplet and does not exceed 20% close to the ice-water interface. Similar errors on a freezing solid-liquid interface are found by Voulgaropoulos et al. [59].

The LIF measurements were implemented in this work in order to provide information on the rates of droplet freezing. The dye-doped water fluoresces, appearing bright on the images, while the ice and oil appear dark. We developed an in-house based algorithm that can track the displacement of the solid-liquid

interface in time in the MATLAB environment. The method is based on the intensity gradients of neighbouring 8-bit pixels. An adaptive binarisation algorithm is applied to the raw images (Figure 3(A)), which are then segmented by separating the droplet from the background and locating the solid-liquid interface (Figure 3(B)). The final interface is then obtained as the perimeter of the segmented area (Figure 3(C)). The results can be reproduced experimentally within a variation of ±10%.

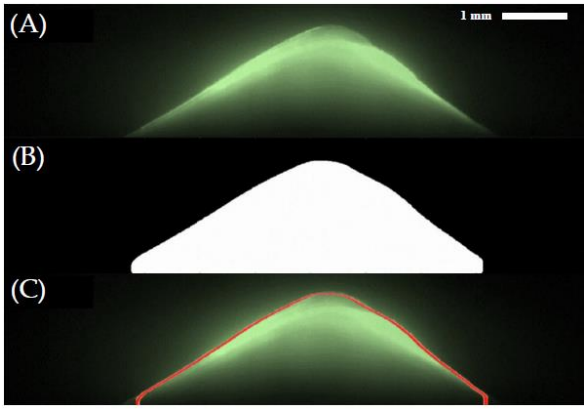

Figure 3. An illustration of the application of the image analysis algorithm employed on the planar laser-induced fluorescence (PLIF) images to obtain the water-ice interface profile over time: (A) raw image, (B) binarised image, and (C) interface detection (red line).

3. Numerical methods

Based on the literature review in the introduction section, the supercooling stage can be modelled by solving governing equations of natural convection without phase change. The assumption of uniform temperature could be used to calculate the transient temperature at the supercooling stage by utilising heat balance [4,6]. A global energy balance could also be used to evaluate the ice mass fraction at the end of the recalescence stage [4,6,60,61]. Therefore, the thermophysical properties of the resulting water-ice mixture can be obtained.

In this study, it was assumed that the volume of the droplets does not change during the freezing process. In addition, it was assumed that the difference between the freezing temperature and the supercooled temperature water is small, which excludes the nucleation/recalescence stages from the calculations. These assumptions are supported by experimental observations. In most of the experiments performed in this study, the subcooling time was less than 1% of the total freezing time. A similar assumption was also used by Karlsson et al. [56,57]. The numerical model was developed based on the thermo-fluid dynamics of freezing which accounts for natural convection, conduction, and phase change. The enthalpy-porosity formulation was employed for modelling the solidification process of the water droplet.

3.1. Governing equations

In the enthalpy-porosity method, the liquid-solid interface (known as the "mushy" zone [62]) is treated as a porous zone where the porosity equals the liquid fraction. In order to consider the effect of the droplet pressure induced by the solid interface, appropriate momentum sink terms are added to the momentum equations. In the computation domain, each cell is associated with the liquid fraction calculated based on an enthalpy balance. The mushy zone is modelled as a "pseudo" porous medium within which the liquid fraction, and, therefore, the porosity and velocity decrease to zero as the material solidifies in a cell. It is assumed that the fluid is incompressible and Newtonian, and that its flow is two-dimensional, laminar, and transient. Since the velocity gradient in the freezing process of water droplets is not large, viscous dissipation was neglected. Following the approach implemented by Kadivar et al. [63], a linear variation of the liquid fraction with temperature was also assumed, and the following governing equations are considered:

1) Continuity:

$$\frac{\partial \rho}{\partial t} + \nabla.(\rho \vec{v}) = 0, \tag{1}$$

where ρ denotes the density, $\vec{v}$ is the velocity field, and t represents time.

2) Momentum:

$$\frac{\partial(\rho \vec{v})}{\partial t} + \nabla.(\rho \vec{v}\vec{v}) = -\nabla P + \nabla.(\mu \nabla \vec{v}) - \rho \mathrm{g} + \frac{(1-\chi)^2}{\chi^3 - \varepsilon}\vec{v} A_{\mathrm{mush}}, \tag{2}$$

where P is the pressure, T is the temperature, and μ dynamic viscosity, g is the gravitational acceleration, β is the coefficient of thermal expansion, ρ is the liquid density, and the liquid fraction χ is defined as:

$$\chi = \begin{cases} 0 & T < T_{\mathrm{solidus}} \\ \frac{T - T_{\mathrm{solidus}}}{T_{\mathrm{liquidus}} - T_{\mathrm{solidus}}}; & T_{\mathrm{solidus}} < T < T_{\mathrm{liquidus}} \\ 1 & T > T_{\mathrm{liquidus}} \end{cases}. \tag{3}$$

For a pure substance $T_{\mathrm{solidus}} = T_{\mathrm{liquidus}}$, however, this assumption can sometimes trigger fast solidification/melting. Therefore, in some cases, a small difference between these two values is considered. Theoretically, a smaller difference can provide a more precise solution, although the nonlinearity of the problem also becomes prominent since the thermal properties vary sharply near the freezing temperature. A temperature difference of 0.2 K was considered for this study which was suggested by Zhang et al. [43].

The last term on the right-hand side of the momentum equation is a source term, sought to reproduce porosity in the mushy zone based on the enthalpy-porosity approach. The constant ε is a small number (taken to be $\varepsilon = 0.001$) to prevent division by zero as χ tends to zero during solidification [63,64]. The

term A_{mush} is a constant reflecting the mushy zone morphology that describes how steeply the velocity is reduced when the material solidifies. The influence of the value of A_{mush} was also investigated by performing freezing simulations using three different values of A_{mush}, i.e., 10^4, 10^5, and 10^6. It was found that the value of 10^5 is a suitable value in terms of results stability for this study, which is also the default value of ANSYS-Fluent and recommended by several studies, e.g., see Kadivar et al. [63].

Due to the small variations in density, the Boussinesq approximation was used to calculate the variation of the density. The Boussinesq approximation is accurate as long as changes in actual density are small, which is a valid assumption in freezing processes. Based on this approximation, the fluid density is modelled as:

$$\rho = \rho_0[1 - \beta(T - T_0)] \tag{4}$$

where ρ_0 and T_0 are the reference density and temperature of liquid.

3) Energy:

$$\frac{\partial}{\partial t}(\rho h) + \nabla.(\rho \vec{v} h) = \nabla.(k \nabla T)\ , \tag{5}$$

where *k* is the thermal conductivity, and *h* the total volumetric enthalpy, that is the sum of sensible enthalpy, h_s, and enthalpy of fusion (latent heat), h_{fs}:

$$h = h_s + \chi h_{fs}\ , \tag{6}$$

$$h_s = h_{ref} + \int_{T_{ref}}^{T} c_p\, dT\ , \tag{7}$$

where h_{ref} is the sensible enthalpy at the reference temperature, T_{ref} and c_P is the specific heat capacity.

The thermophysical properties of the ice, water and silicon oil, as used in the present work, are listed in Table 1. The properties of water and ice were adopted from Ref. [65], and those of the oil were taken from the manufacturer's datasheets. Apart from the density that is approximated by Eq. (4), other thermophysical properties are evaluated by interpolating between temperature for quantities presented in Table 1.

Table 1. Thermophysical properties of ice, water, and silicon oil.

	T (K)	Heat capacity (J/kg.K)	Thermal conductivity (W/m.K)	Viscosity (mN.s/m^2)	Thermal expansion coefficient $\times 10^{+3}$ (1/K)	Latent heat of fusion (kJ/kg)
Ice	253	1945	2.03	-	-	-
	273	2040	1.88	-	-	-

Water-liquid	273.15	4217	0.57	1.75	-0.068	333.6
	275	4211	0.57	1.65	-0.033	-
	280	4198	0.58	1.42	0.046	-
	285	4189	0.59	1.23	0.114	-
	290	4184	0.60	1.08	0.174	-
	295	4181	0.61	0.96	0.228	-
Oil	273.15	1700	0.14	1.63	1.060	-

3.2. Numerical procedure

Before the numerical procedure is discussed, a schematic illustration of terms that regularly are referred to in the upcoming sections is demonstrated in Figure 4. This figure illustrates a sessile water droplet with a radius of r_d surrounded by silicone oil. In order to evaluate the temporal evaluation of the ice formation, the freezing front (r_f) is traced along the y axis and then compared with the experimental results. Figure 4 also shows the sessile liquid water enclosed inside the ice dome that is partially formed over it.

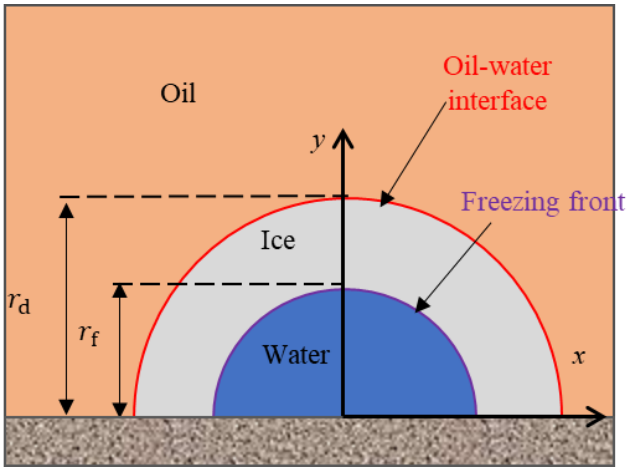

Figure 4. Schematic of a sessile droplet sitting on a horizontal surface, where r_d is the radius of the sessile droplet, and r_f is the thickness of the freezing front.

Figure 5 shows a schematic of the considered computational domain where due to symmetry, only half a water droplet surrounded by silicone oil with a temperature below the water freezing point was modelled. The solidification process (including natural convection, conduction and phase change) was modelled inside the water droplet, while merely the natural convection heat transfer was considered in the oil. It was assumed that the effect of surface tension is negligible, and that the shape of the sessile droplet on the surface is hemispherical, with a contact angle of 90 °between the droplet and the surface. It was also assumed that the

shape of the sessile droplet (and consequently the volume of the droplet) did not change during the solidification process. The boundary conditions considered in this study are also shown in Figure 5.

For the sake of saving computational resource and time while retaining an acceptable penalty on the accuracy of numerical results, the simulation of free convection in the oil phase was decoupled and performed separately from that of the freezing of the water droplets. As schematically illustrated in Figure 5, the oil and water domains are decoupled at their interface, resulting in two separate and successive CFD simulation steps:

Step (i): steady-state free convection in oil with a domain size of $L \times L$; and,

Step (ii): transient freezing of water in a sessile droplet with a radius of r_d.

In the first step of simulation (Step (i)), a steady-state free convection flow in the oil domain was simulated, considering a constant temperature of 273.15 K (freezing temperature of water) at the water-oil interface. The assumption of constant temperature at the interface is a valid assumption owing to the freezing process. This simulation led to capturing the spatially dependent profile of heat transfer coefficient $\lambda(x, y)$ of oil over the droplet. In the second stage of simulation (Step (ii)), the heat transfer coefficient profile $\lambda(x, y)$, captured in Step (i), was implemented to simulate transient freezing of water in a sessile droplet.

The heat transfer coefficient profile $\lambda(x, y)$ along with the oil temperature T_{oil} is considered by implementing a convective boundary condition over the outer surface of the droplet in Step (ii) of simulation in Figure 5 (c). The convective boundary condition is defined as:

$$-k\nabla T|_{\text{interface}} = q_v, \tag{8}$$

$$q_{\text{v}} = \lambda(x, y)\,(T_{\text{oil}} - T_w) \tag{9}$$

where q_{v} is interfacial convective heat flux, while T_{w}, and T_{oil} are the temperature of the droplet surface and the oil temperature, respectively. Other boundary conditions used in the simulations are shown in Figure 5. A no-slip boundary condition was applied on the adiabatic walls and interface for the momentum equation.

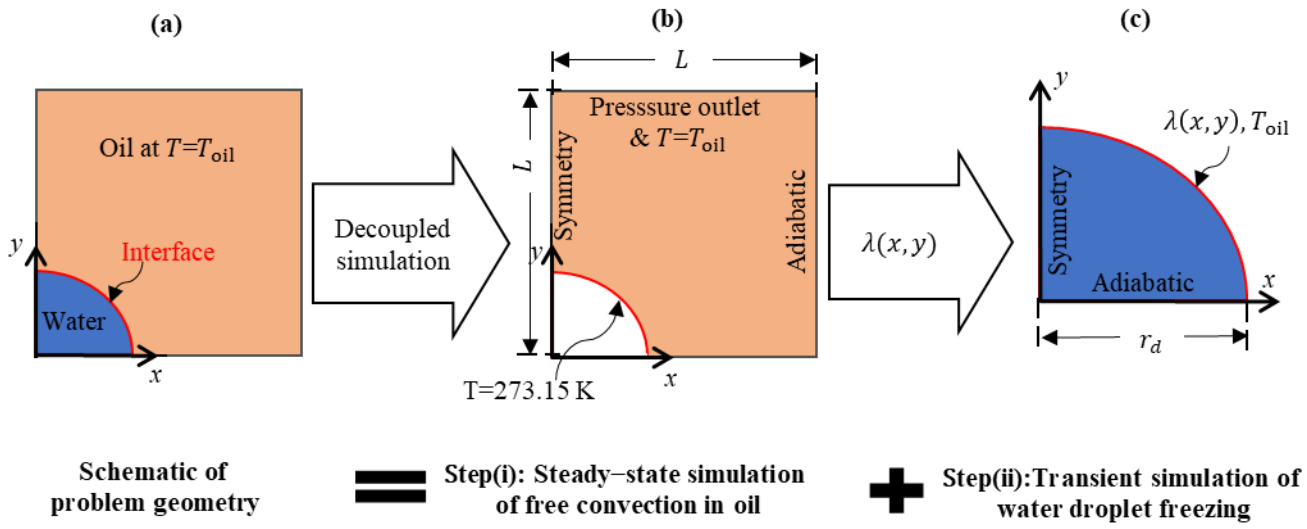

Figure 5. Schematic of decoupled CFD simulation steps: (a) schematic of problem geometry including oil and water in contact, (b) geometry and boundary conditions used for steady-state free convection simulation of oil with a domain size of $L \times L$, and (c) geometry and boundary conditions considered for transient simulation of water freezing in a sessile droplet with a radius of r_d, where λ(x,y) is a spatially-dependent profile of heat transfer coefficient of oil on the surface of the water droplet at the interface.

ANSYS-Fluent 19 was employed for solving the set of coupled governing partial differential equations presented earlier in Section 3.1. Based on the control volume technique, the "coupled" algorithm was used for treating the pressure-velocity coupling. The "coupled" algorithm solves the momentum and pressure-based continuity equations together through an implicit discretisation of pressure gradient terms in the momentum equations and an implicit discretisation of the face mass flux, including the Rhie-Chow pressure dissipation terms [66]. The discretisation of momentum and energy equations was performed using the second-order differencing scheme. A second-order implicit time-advancing method with a timestep of 0.01 s (as concluded in the next section) was used. A course of 60 iterations at each timestep was found satisfactory to fulfil the convergence criteria of less than 10^{-6} for all equations. In order to achieve a stable solution, all under-relaxation factors were modified and adjusted during the simulations [63].

3.3. Grid study and validation

The accuracy of the numerical simulation depends on the general factors, including the resolution of the computational grid, timestep, size of the computational domain. Since the droplet is cooled through natural convection heat transfer to the oil, the size of the computational domain is also critical. The domain size must be large enough to eliminate the effect of the boundaries (end-effects) on the numerical results. To study the dependency of the simulation results on the grid resolution, domain size and timestep, 6 cases

comprising different combinations of these contributing factors, listed in Table 2, were simulated. In that regard, the trend of freezing layer thicknesses of those cases with time are displayed in Figure 6.

Table 2. Case studies for computational grid resolution, timestep and computational domain size.

Simulation	Number of computational cells	Domain size (L/r_d)	Timestep (s)
Case 1	17725	19	0.1
Case 2	39952	27	0.05
Case 3	39952	27	0.01
Case 4	39952	38	0.01
Case 5	632110	38	0.01
Case 6	1275600	46	0.005

Among these three contributing factors, the timestep size has the most decisive influence on the numerical results. The next influential factor on the numerical results was found to be the domain size. Since the water droplet was surrounded and cooled by oil through natural convection, the domain size can significantly influence the natural convection dynamic in the oil. According to Figure 6, for this study, the numerical results become independent of the mesh resolution and timestep for a computational domain with an L/r_d = 38 comprising 632110 computational cells and a constant timestep of 0.01 s. Considering r_d = 2.60 mm, the computational domain with an L/r_d = 38 is attributed to a box of about 100 mm × 100 mm, which is also the size of the box in the experiment. Figure 7 shows the computational grid generated for the simulation of the water and oil domains.

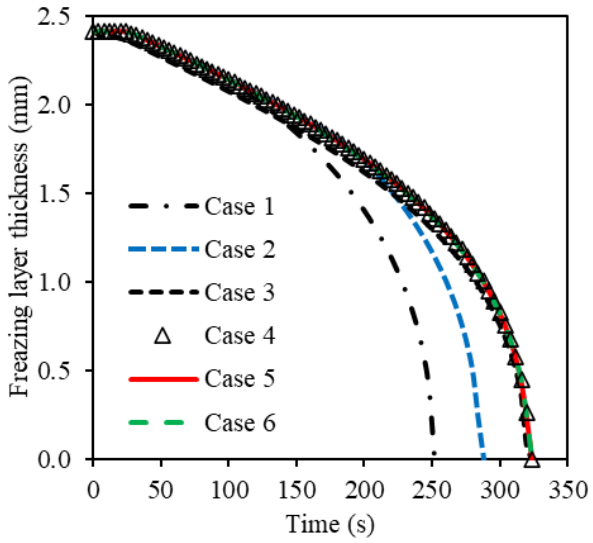

Figure 6. Effect of grid resolution, domain size and timestep size on the freezing layer thickness for a sessile water droplet with a diameter of r_d = 2.60 mm surrounded by cold silicone oil at T_{oil} = 260 K. The description of each case is listed in Table 2.

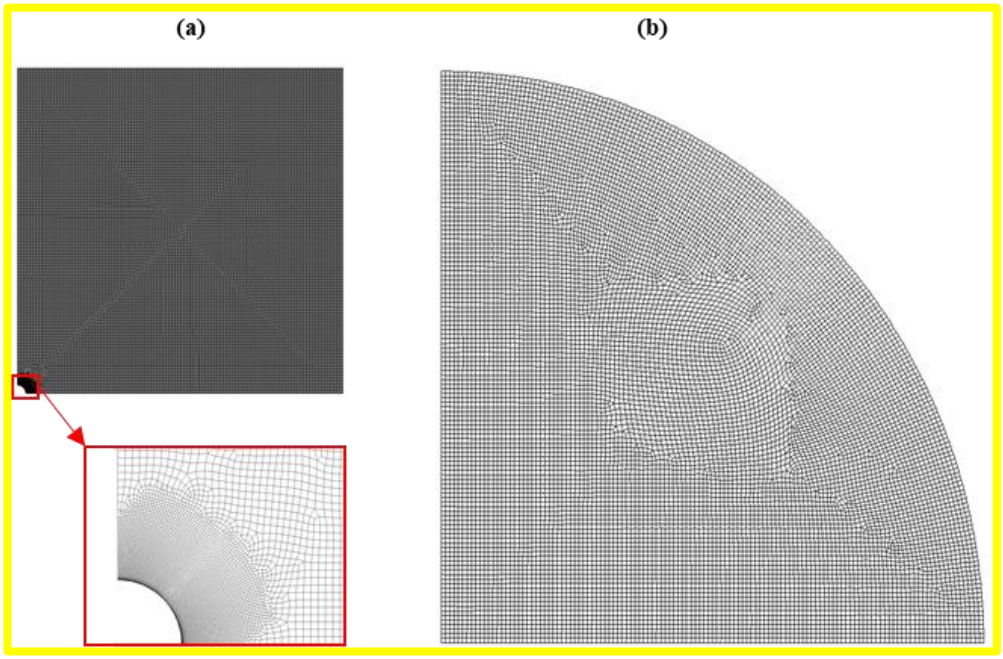

Figure 7. Computational grids for Case 5 in Table 2: (a) for the steady-state free convection simulations in the oil phase, corresponding to Figure 5(b); and (b) for the transient simulation of water freezing in a sessile droplet with r_d = 2.60 mm corresponding to Figure 5(c).

In Figure 8, we compare numerical predictions of the thickness freezing front, which is tracked along the streamwise axis (vertical centreline shown in Figure 4) of the droplet, against experiments. This figure shows good agreement between the experimental data and numerical results. Since it was assumed that the volume of the droplet is constant during numerical simulation, small deviations between numerical and experimental data were observed at the beginning of the freezing stage of large droplets (blue curve in Figure 8). The observed discrepancy is attributed to several factors the complexity of phenomena involved in experiments, such as:

- complexity in the nucleation sites, including their number, location, etc.;
- the asymmetric nature of the problem; and,
- the uncertainty in the measurement of the droplet diameter.

The impact of these factors and the CFD simulation assumptions (e.g., the assumption of no volume change in the CFD) become more significant for larger droplets than smaller ones. For example, as shown in Figure 8, the average discrepancy for the smallest droplet (D = 1.71 mm) was found at 1.2% compared to 8.0% for the largest droplet (D = 3.86 mm). It is noted that, in this figure, the maximum discrepancies for the smallest and largest droplet are about 3% and 18%, respectively.

The asymmetrical results captured in the experiments (Figure 9) were not depicted in the CFD results as the simulations were based on symmetrical modelling (only half of the droplet modelled). However, for the sake of better comparison, the CFD results were mirrored (to show the whole droplet) and printed in black background with the phosphoric green region for solidified water droplets. The CFD results were also qualitatively and quantitively compared with experiments in Figures 8 and 14, respectively.

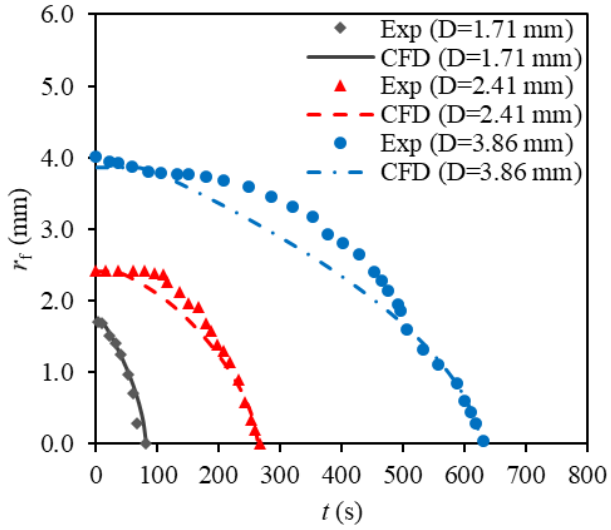

Figure 8. Validation of numerical data against the experimental results for sessile water droplets with different diameters from D = 1.71 mm to 3.86 mm surrounded by silicone oil at a temperature of T_{oil} = 260 K.

4. Results and discussion

4.1. Phenomenology

The characteristics of freezing were quantified over a range of conditions spanning a range of diameters from D = 1.7 mm to 4.5 mm and oil temperatures from T_{oil} = 260 K to 270 K. Two typical cases for a water droplet with a diameter of 3.9 mm are shown in Figure 9(A-G) for an oil temperature of T_{oil} = 260 K and Figure 9(H-N) for T_{oil} = 270 K, respectively.

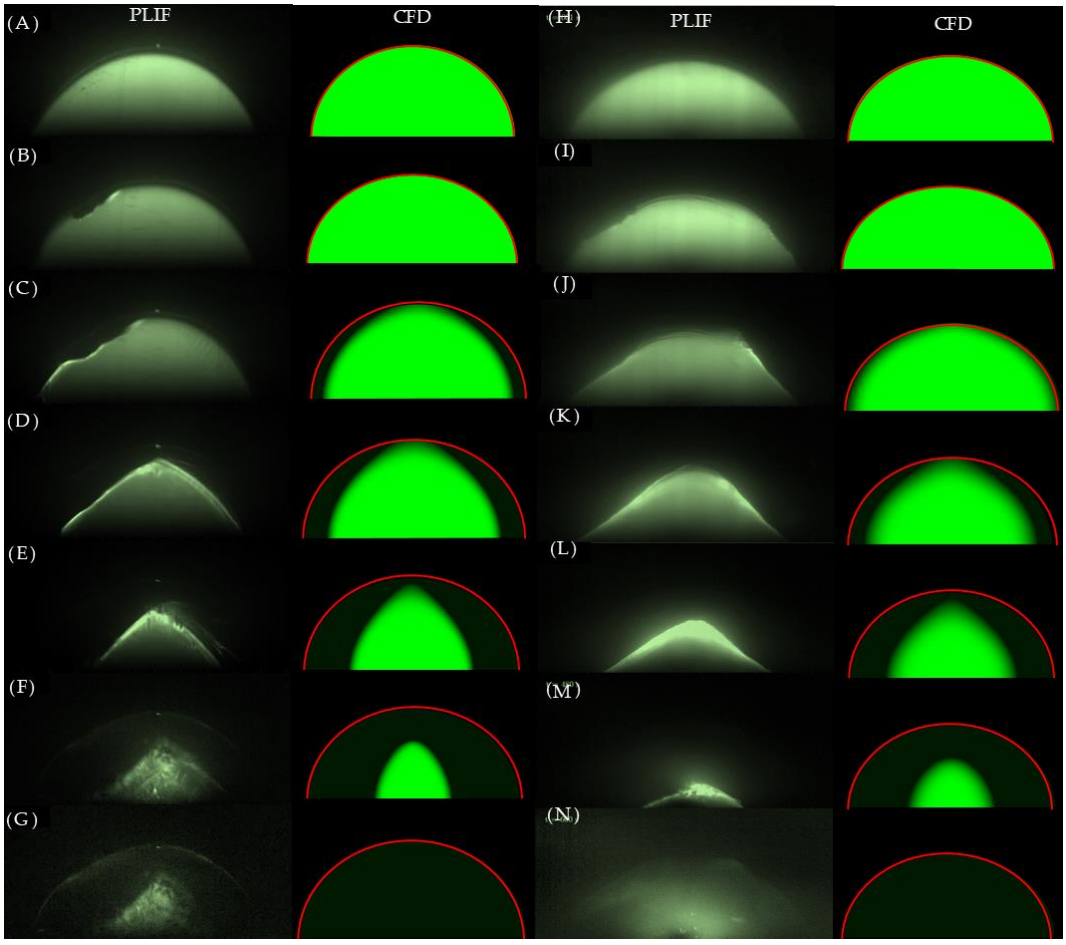

Figure 9. Planar laser-induced fluorescence (PLIF) images (left) and mirrored CFD results (right) of a freezing sessile water droplet with a diameter of D = 3.9 mm, surrounded by cold silicone oil at: (A-G) T_{oil} = 260 K, and (H-N) T_{oil} = 270 K. The corresponding times are: (A), (H) t^* = 0; (B), (I) t^* = 0.1; (C), (J) t^* = 0.2; (D), (K) t^* = 0.4; (E), (L) t^* = 0.6; (F), (M) t^* = 0.8; (G), (N) t^* = 1. The dynamic range of each PLIF image has been adjusted for clarity. The red lines in the CFD results depicts the border of the droplet.

It is noted, from Figure 9, that the contact angle appears to change slightly as the droplet cools, before it freezes and the ice dome forms, and that its value is smaller than 90 ° once freezing is initiated. This

contrasts with the simulations, where the contact angle was considered constant at 90 °. The experiments did not allow an accurate *in situ* measurement of the contact angle over the entire lifetime of the phenomenon (illustrated in Figure 1). Nevertheless, the reasonable agreement in both trends and values between the CFD predictions and experiment date that are shown further down in this section give some confidence that contact angle variations are small enough not to affect the main results and conclusions.

The time instances shown are indicated by a normalised time, which is simply defined as the ratio of the time over the total freezing time, i.e., $t^* = t / t_f$. Freezing was initiated from either one or multiple locations around the droplet. The sides of the droplets were found to be the most favourable, as freezing was statistically observed to be initiated in these regions more frequently. This finding can be related to the inner natural convection patterns and resulting temperature field of the droplet during the cooling and before the freezing starts, which will be discussed further in this section. The final volume of the ice was larger than the initial volume of the water droplet, as expected by the density changes during the phase change of water to ice. No singularity point was observed at the tip of the water droplet, possibly because the freezing was initiated from the surrounding interface, instead of from a plate at the bottom of the droplet. Tip singularities are commonplace in experiments where the freezing of droplets resting on cold plates occurs [34,45,67], but has not been reported, to the authors' best knowledge, for systems such as those investigated herein. Several phenomena are observed from the PLIF, as shown in Figure 9. For the case of Figure 9(A-G) corresponded to a temperature of about 30 K below the ambient temperature, freezing started from the right-hand side of the droplet and wrinkling of the interface is observed on the opposite side of the drop (Figure 9(C), PLIF). The asymmetry is expected in an experiment due to the stochastic nature of the nucleation. At t = 60 s (Figure 9(C), PLIF), freezing has also started from the right-hand side of the drop, and both fronts propagate towards the bottom. The total duration of freezing was about 300 s. For the case of Figure 9(H-N) recorded for a smaller temperature difference of about 20 K compared to ambient, the freezing is initiated more symmetrically, as shown for t = 60 s (Figure 9(I)). Wrinkling patterns appear at the top of the droplet until a peak forms at $t \sim 240$ s (Figure 9(J)). The droplet has completely frozen at t = 620 s, much longer than the case of Figure 9(A-G), and the final shape of the ice has deformed and lost its curvature compared to the initial semi-spherical water droplet.

The case of Figure 9(A-G) was recorded and modelled for a temperature difference of about 30 K, compared to ambient. The wrinkling observed in Figure 9(C) can be attributed to wide pressure gradients forming inside the droplet and momentum effects as the ice displaces the water phase downward at the centre of the droplet. The observed wrinkling in the PLIF images of Figure 9(C) can be explained by the detailed CFD results illustrated in Figure 10. This figure includes the pressure contours at the left-hand side, while the velocity field overlaid with velocity vectors are shown on the right-hand side of Figure 10. At t^* = 0.1, the freezing starts

from the low-velocity region of the droplet, which causes the pressure at the bottom corners of the droplet to be higher than the other part of it. In the experiments, due to the stochastic location of the nucleation sites in the droplet, the freezing was initiated in different regions of the droplet in different experiments. However, in the CFD, the freezing begins from the low-velocity region in the droplet. At the beginning of freezing (as shown in Figure 11, $t^* = 0.1$), the high-temperature difference increases the buoyant force in the droplet, forming a strong recirculation region inside the droplet and consequently low-pressure area at the centre of the droplet. The formation of pressure gradient inside the droplet (as shown in Figure 10) and the volume change of water during the freezing process triggers wrinkle formation at the water and oil interface. Further experimental investigations require to verify this justification and reasoning. The wrinkling was not observed in CFD due to the assumption made in the simulations, as discussed earlier.

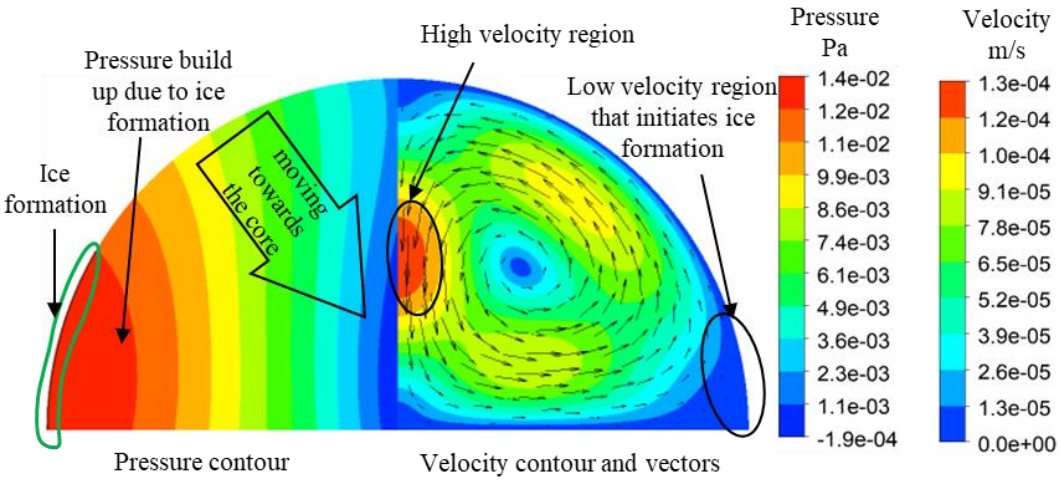

Figure 10. Instantaneous pressure field contours (left) and velocity field maps (right) from CFD for a freezing water droplet with a diameter of D = 3.9 mm surrounded by silicone oil at a temperature of T_{oil} = 260 K. The results correspond to the experiment in Figure 9(B) at t^* = 0.1.

Figure 11 indicates mirrored CFD results of temperature distribution inside the water droplet at different timesteps while the droplet is surrounded by cold silicone oil at T_{oil} = 260 K. The black line in each image shows the freezing front (moving ice-water interface). At the commencing instance (t^* = 0.1), the freezing front initiates from the bottom wall and, as time passes, gradually propagates both circumferentially and radially until the tip of the droplet freezes, and the liquid water is enclosed inside a dome of ice (see Figure 11, t^* = 0.4 and t^* = 0.6). Once the closed dome formed, the freezing of water occurs inside a dome of ice, and ice presents a thermal resistance between liquid water and oil at later times (t^* = 0.4 and 0.6). At the beginning of freezing (t^* = 0.1), the ice dome has not been formed, and the liquid water is in contact with the surrounding oil; thus, a wide temperature distribution is observed, ranging from 273.15 K (approximately the freezing point of water) to 277.9 K. As the t^* increases, the ice dome forms which acts as an insulator.

Consequently, the temperature difference in the water droplet rapidly decreases and remains unchanged until the end of the freezing process. The large temperature difference at the beginning of the freezing stage leads to a wider density gradient compared to the rest of the freezing process. Therefore, stronger free convection and higher solidification rate are anticipated at the beginning of the freezing stage.

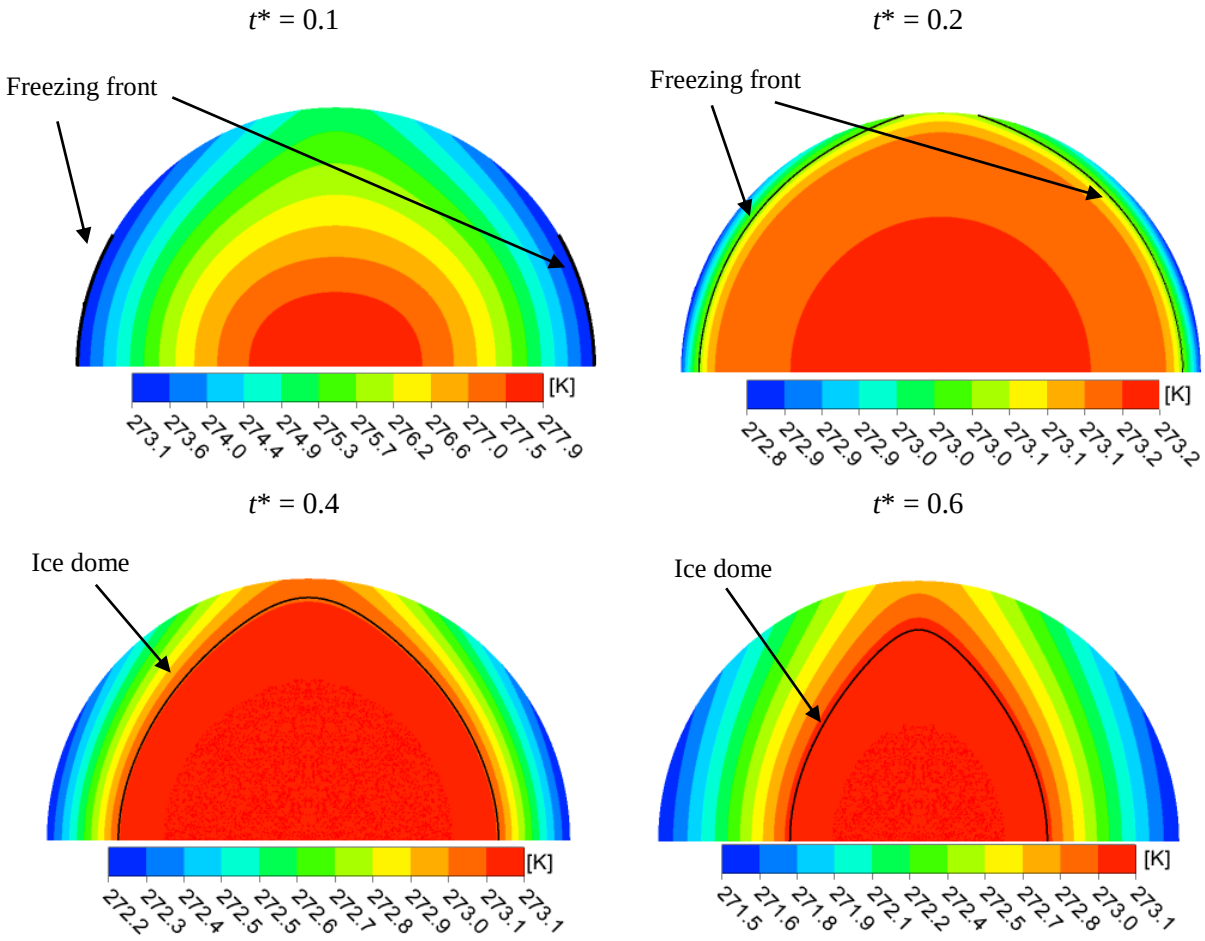

Figure 11. Instantaneous mirrored temperature fields from CFD for a freezing water droplet of volume with a diameter of D = 3.9 mm surrounded by silicone oil at a temperature of T_{oil} = 260 K. The black lines are the freezing front, and the coloured contours are the temperature distribution. The results correspond to the experiment in Figure 9(B-E).

Figure 12 illustrates mirrored CFD results of pressure distribution inside the water droplet at different timesteps while the droplet is surrounded by cold silicone oil at T_{oil} = 260 K. The black line in each image shows the freezing front. Therefore, at the beginning of freezing (Figure 12, t^* = 0.1), when the ice dome is not formed, and the liquid water is not enclosed yet, the ice formation and momentum transfer due to buoyancy force inside the droplet starts to build up pressure at the bottom corners of the water droplet. Indeed, as the ice formation sprouts, momentum transfer and recirculation of fluid due to free convection occur (see also Figure 10), which

lead to a low-pressure zone core at the centre of the droplet (the central blue regions in Figure 12). As time passes and the freezing area grows (Figure 12, $t^* = 0.2$), the high-pressure zone propagates towards the centre of the water droplet, and the negative pressure zone is being suppressed. Once the closed dome forms (all the outer surface of the water droplet freezes at later instances ($t^* = 0.4$ and $t^* = 0.6$)), the liquid is being trapped in the centre of the solid part of the droplet which leads to pressure built up underneath the dome.

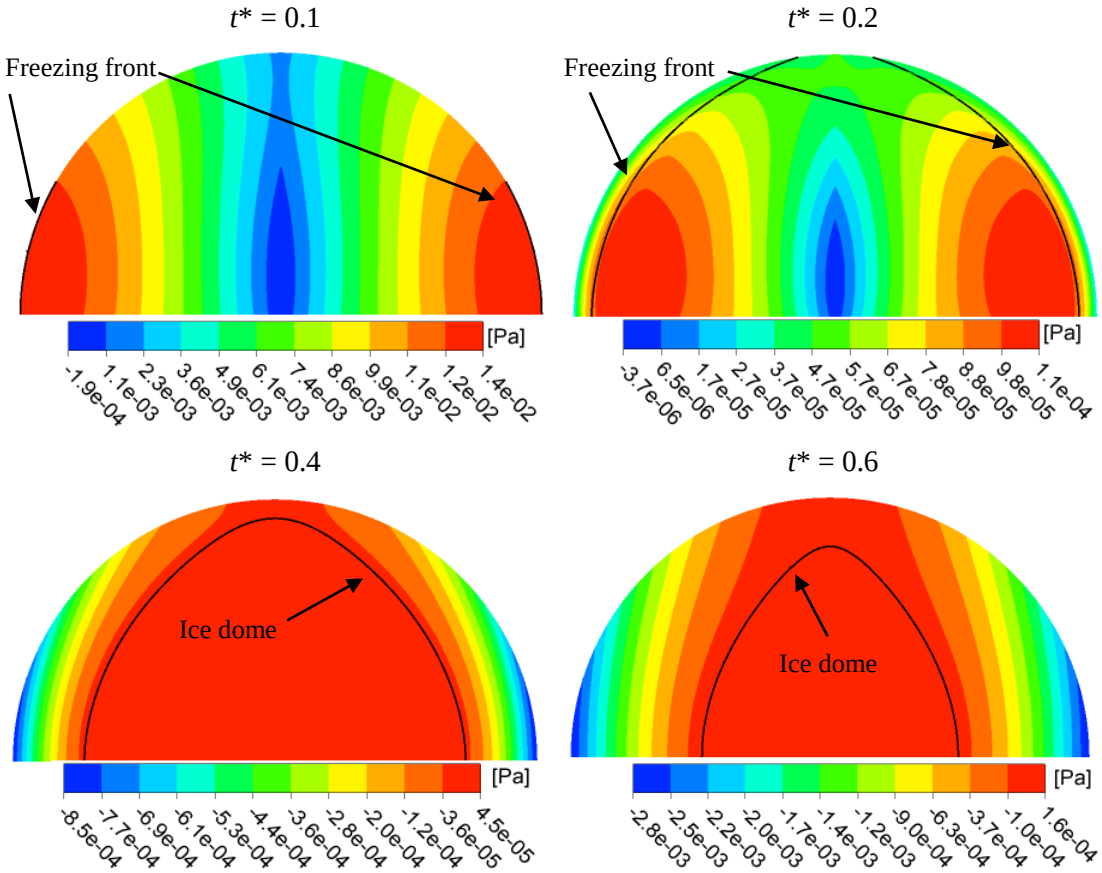

Figure 12. Instantaneous mirrored pressure fields from CFD for a freezing water droplet with a diameter of $D = 3.9$ mm surrounded by silicone oil at a temperature of $T_{oil} = 260$ K. The black lines are the freezing front, and the coloured contours are the pressure distribution. The results correspond to the experiment in Figure 9(B-E).

4.2. Freezing rates

The ice-water interface was tracked along the vertical centreline of the droplet for various conditions. The radius of the frozen fluid (r_f), normalised by the droplet radius (r_d), is plotted in Figure 13 as a function of normalised time for three droplets of different size (equivalent diameters). As a complementary study, the non-normalised freezing rates of the same cases are displayed as an inset. All three cases were performed experimentally at $T_{oil} = 260 \pm 0.5$ K.

The dynamics were similar for the three cases shown in Figure 13. The ice growth followed an exponential trend regardless of the droplet size. While this trend did not appear to be affected by the size of the droplet, the actual time for the complete freezing of the droplet increased by almost an order of magnitude as the droplet size doubled (see the inset of Figure 13). This finding has significant implications for applications involving emulsification, oil-water separation, and crystallisation processes, e.g., in the design of anti-icing system and preventing contamination and corrosion [68]. Figure 13 demonstrates an acceptable agreement between the CFD results and experimental data, with some observed deviations at the beginning of the freezing stage of large droplets. An explanation for the observed discrepancies between the CFD and experimental results was given in Section 3.3.

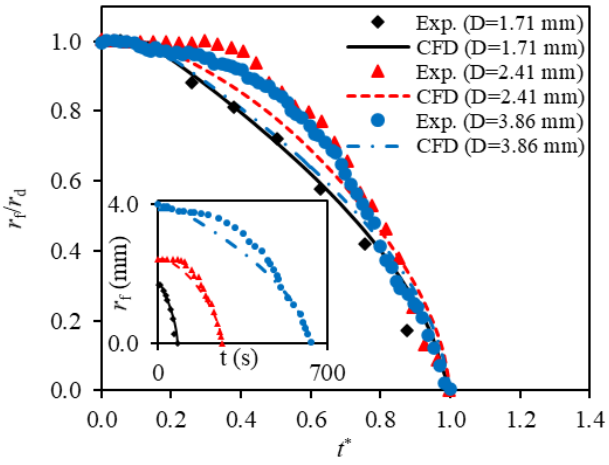

Figure 13. Normalised freezing dynamics, i.e., reduction in liquid phase (water) radius over time, from both experiments and CFD for freezing water droplets over a range of diameters from D = 1.71 mm to 3.86 mm surrounded by silicone oil at a temperature of T_{oil} = 260 K. Results are in the vertical direction along the centreline. The insert saw raw results of liquid-phase radius before normalisation.

Figure 14 shows experimental and CFD results of the effect of the oil temperature on the freezing dynamics for a droplet with an equivalent diameter of 2.6 ± 0.3 mm. In the experiments, three oil temperatures were investigated for this purpose, namely 260 K, 266 K, and 270 K. In normalised variables, the trends do appear to remain the same, irrespective of T_{oil}, although the case at 266 K does appear to deviate from the exponential curves. The reason behind this behaviour can be the number of nucleation sites or the temperature of the droplet before nucleation was initiated. In fact, this case was immersed in the oil bath for a longer time (about 15 s) before the homogeneous nucleation started, compared to the average case (which was cooled down for about 2-5 s before nucleation started). It became evident that the cooling time and the initial temperature of the droplet appear to be controlling the freezing dynamics. The same

conclusion can be drawn from the inset of Figure 14. Furthermore, a further 10 K reduction in the oil temperature can reduce the freezing time up to approximately 50 %, as shown in the inset of Figure 14.

CFD results also demonstrated a similar trend as experiments for the three cases shown in Figure 14. The observed deviations between experiments and CFD results in Figure 14 explained earlier in Section 3.3. For the results correspond to the silicon oil with lower temperatures (266 K and 270 K), the discrepancies observed before the end of the freezing could also be due to the exclusion of the supercooling time in the CFD model.

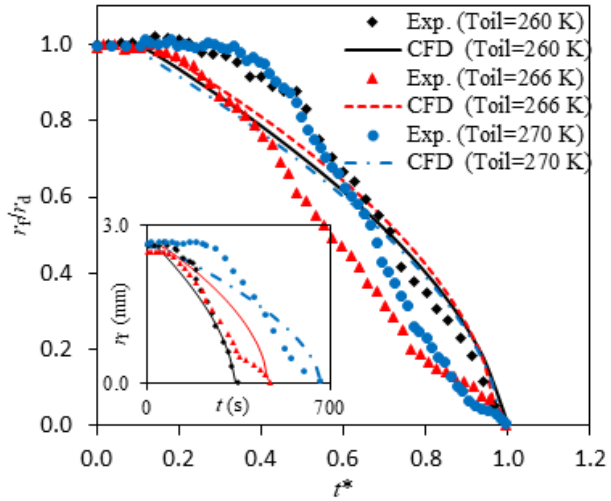

Figure 14. Normalised freezing dynamics, i.e., reduction in liquid phase (water) radius over time, from both experiments and CFD for freezing water droplets of diameter D = 2.6 mm surrounded by silicone oil over a range of temperatures from T_{oil} = 260 K to 270 K. Results are in the vertical direction along the centreline.

4.3. Free convection in the silicone oil

As discussed in Section 3.2, the steady-state CFD model was used to simulate free convection heat transfer in silicone oil. The results were also employed to calculate the spatially-dependent profile of heat transfer coefficient $\lambda(x,y)$ of oil on the surface of the water droplet, as shown in Figure 5. In this section, the interfacial convective heat flux calculated by Eq. (9) is used to study free convection in silicone oil. Figure 15 display steady-state CFD simulations of free convection in silicone oil at a temperature of T_{oil} = 260 K surrounding droplets with a range of diameters from D = 1.71 mm to 3.86 mm. The circumferential position φ on the horizontal axis of this figure varies from φ = 0 ° (where the surface of the droplet sits on the solid surface) to φ = 90 ° (the tip of the droplet). As the droplet diameter decreases, the circumferential heat flux distribution over the droplet's surface increases significantly. This result is aligned with the drawn conclusion of experimental findings, which as the droplet size (diameter) doubles, the time required for the droplet to completely freeze increases by almost an order of magnitude for the range of conditions investigated (see discussion on Figure 13).

Another interesting conclusion was the trend of circumferential heat flux. As shown in Figure 15, the maximum heat flux occurs near the solid surface (at smaller φ). This can justify why solidification sprouts at the initial time close to the solid surface (see the freezing front at $t^* = 0.1$ in Figures 11 and 12). In addition, the location of the maximum heat flux depends on the droplet size. For example, for droplet with diameters D = 3.86 mm, 2.41 mm and 1.71 mm, the maximum heat flux occurred at $\varphi \approx 10°$, $\varphi \approx 15°$ and $\varphi \approx 20°$, respectively. The heat flux drops beyond the maximum heat flux angle until it reaches the tip of the droplet ($\varphi = 90°$), where the heat flux is minimum due to the natural convection plume formed in the oil over the tip of the droplet. This behaviour is also shown in the freezing fronts in Figures 11 and 12 at $t^* = 0.1$ and 0.2, where during the formation of the ice dome, the tip of the droplet ($\varphi = 90°$) is the last location, where the ice forms. Another conclusion from this image concerns the significant variation between the maximum and minimum circumferential heat fluxes on the surface of the 1.71 mm droplet compared to the larger droplets. This result also is useful for industrial applications, e.g., finding optimum droplet sizes for boosting heat transfer and optimising the solidification time of systems according to the needs of specific applications.

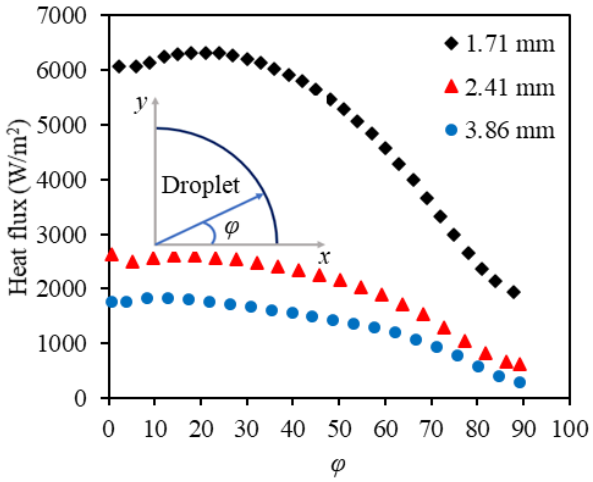

Figure 15. Spatial variation of steady-state interfacial heat flux along the surface of droplets as predicted by steady-state CFD simulations of free convection in silicone oil at a temperature of T_{oil} = 260 K surrounding droplets with a range of diameters from D = 1.71 mm to 3.86 mm.

4.4. Velocity fields

The velocity fields inside the droplet during the solidification of the water droplet were obtained both experimentally with PIV, and numerically. In the experiments, fluorescent tracer particles were used to minimise any reflection effects from the water-oil or ice-water interface. Figure 16 illustrates the resulting planar two-component velocity vector field and the contours of the cross-stream vorticity field for various timesteps. In this case, a droplet of size about 5 mm surrounded by cold oil at T_{oil} = 266 K was considered.

Before solidification starts (t^* = 0), the velocity fields inside the droplet are characterised by natural circulation patterns due to temperature (and hence density) differences between the radially outwards (cold regions in contact with the oil) and inwards (warm regions) locations of the droplet. Two counteracting vortices were observed on each side of the droplet, each with a vorticity peak, as shown in Figure 16. Once freezing was initiated, the pattern slowly changes, and the circulation patterns disappear (t^* = 0.056), dominated by a strong vertical motion towards the bottom of the droplet. This motion was a result of the solidification that takes place on the top of the droplet. Similar findings were recorded in the simulations of Vu et al. [45] for a droplet freezing on a cold plate. In their case, the circulation patterns were formed, although with the counteracting vortices appearing at the top of the droplet. They also observed a strong vertical motion towards the top and away from the freezing front once solidification started.

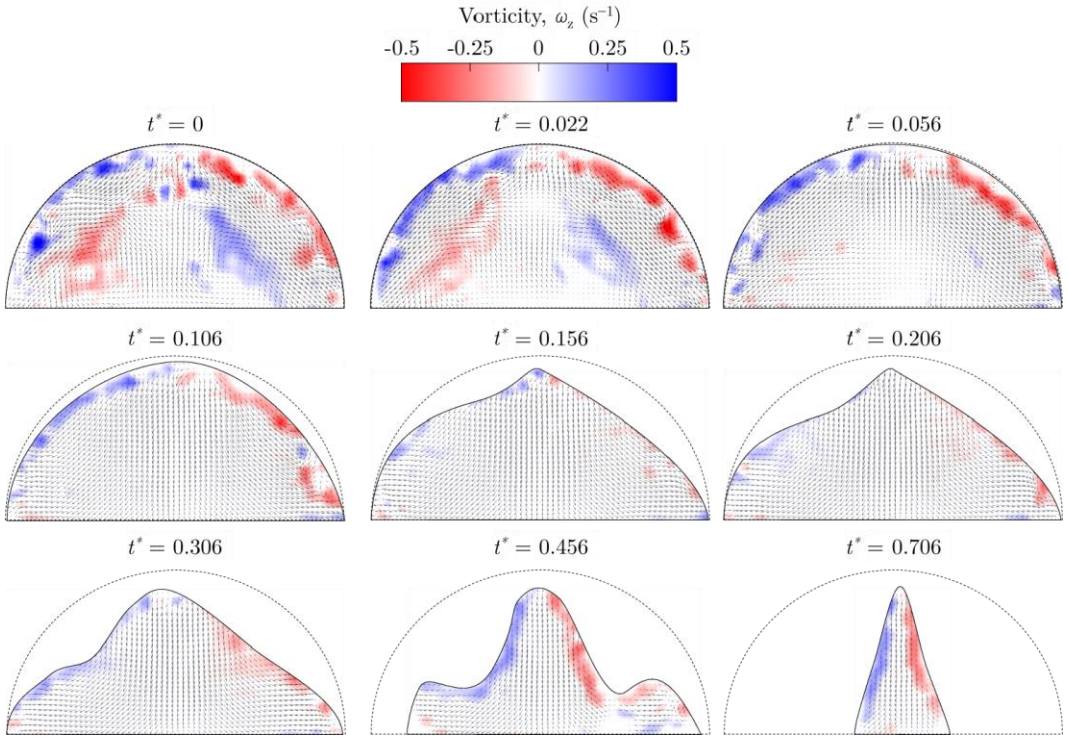

Figure 16. Instantaneous vorticity fields overlaid with velocity vector fields from PIV for a freezing water droplet with a diameter of D = 4.5 mm surrounded by silicone oil at a temperature of T_{oil} = 266 K. The colour-bar denotes the wall-normal vorticity contour values in the maps.

Finally, Figure 17 illustrates the CFD results of velocity contour overlaid with velocity vectors for a freezing water droplet of diameter D = 3.9 mm surrounded by cold silicone oil at T_{oil} = 260 K. These results correspond to the experiment case in Figure 9(B-E). The CFD results also demonstrate two counteracting recirculation regions due to natural convection at the beginning of the freezing stage (t^* = 0.1 and t^* = 0.2). As the freezing front propagates and the ice encompasses the fluid inside the droplet, the centre of the recirculation region

moves toward the top of the droplet and their strength is weakened (t^* = 0.4 and t^* = 0.6). This is mainly due to built-up pressure and diminished temperature distribution in the liquid that lessens the strength of the buoyancy force. In this particular freezing droplet, which has a smaller size compared to what is shown in Figure 17, the circulation patterns do not completely disappear as the freezing continues, although they become significantly weak and dominated by a downward vertical motion of the droplet.

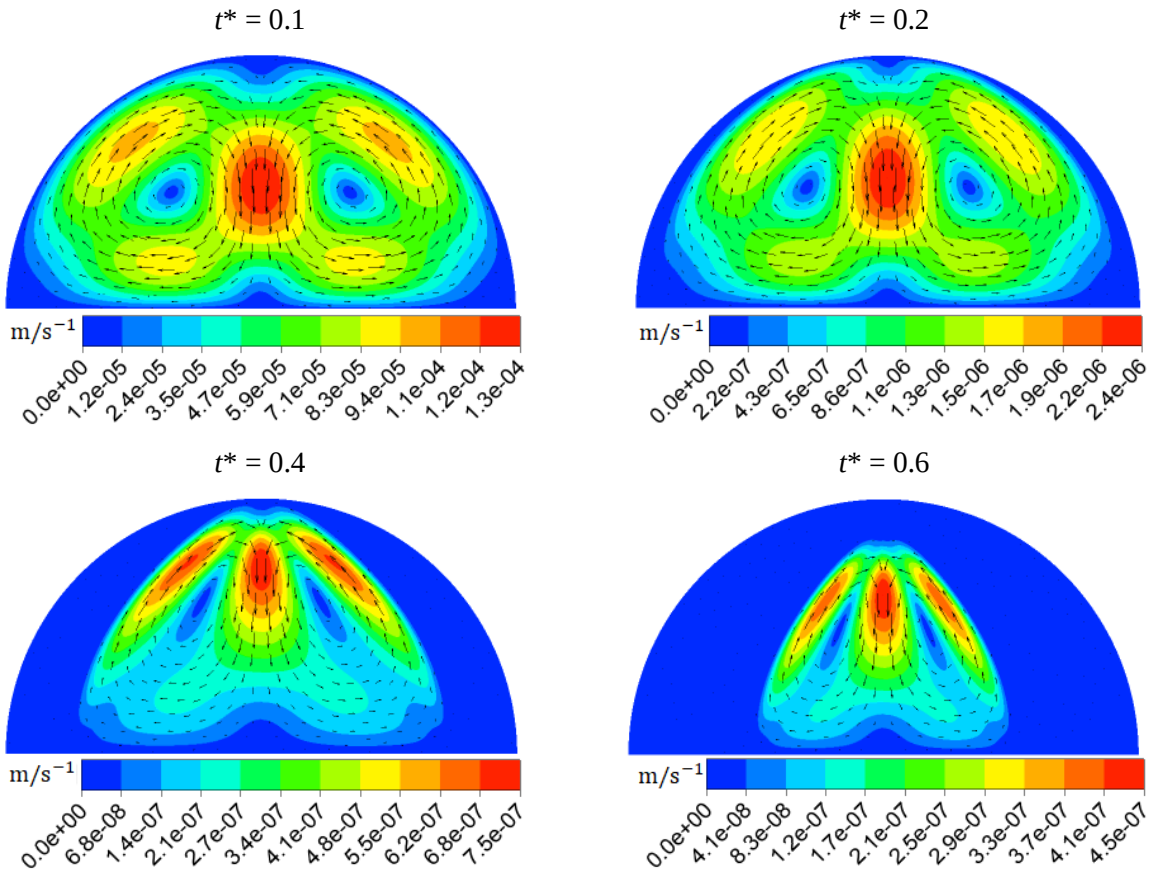

Figure 17. Instantaneous mirrored velocity magnitude contours overlaid with velocity vector fields from CFD for a freezing water droplet with a diameter of D = 3.9 mm surrounded by silicone oil at a temperature of T_{oil} = 260 K. The results correspond to the experiment in Figure 9(B-E).

5. Conclusions

Laser-based diagnostic measurements involving simultaneous LIF and PIV techniques were applied to sessile droplets of water inside an oil-filled glass cuvette, such that the droplets were surrounded by oil maintained at sub-zero temperatures in a free convection arrangement. The experiments aimed to investigate the freezing dynamics of the droplets by capturing the phase, interface and flow-field

characteristics, and were complemented by computational fluid dynamics (CFD) simulations, which showed good qualitative and quantitative agreement with the experimental results. However, slight deviations were also identified, which could be attributed to several factors, including the assumptions considered in the CFD model as well as the phenomena involved in experiments that are difficult to simulate, such as complexity in the nucleation sites with respect to their number, location, etc., and the asymmetric nature of the problem.

The results showed that the droplets froze inwards and in the direction of gravity, a phenomenon which differs from most work in the literature, where solidification arises due to cooling applied below the droplets from a solid plate on which they rest, and the freezing front propagates upwards. An initial buffer period was observed at the droplet centreline, where the ice propagation was very slow (quasi-zero) but increased exponentially after this period. Experimental data showed that the formation of the heterogeneous nucleation sites on the sides of droplets matched with the presence of the main mixing (recirculation) regions before nucleation. The recirculation regions (and, hence, mixing inside the droplet) were suppressed when freezing was initiated.

The CFD results demonstrated a relatively wide temperature and pressure distribution in the water droplet at the beginning of the freezing stage. The ice formation led to pressure build-up in the droplet, suppressing the temperature stratification and considerably weakened recirculation in the liquid region. Accordingly, the droplet freezing process can be divided into two stages; a first stage from the beginning of the freezing until an ice dome formed and a second from ice dome formation until all the liquid froze. A high temperature and pressure distribution were observed inside the droplet in the first stage, and strong recirculation governed the fluid dynamic inside the droplet. As time passed and the ice dome was completed, the liquid water enclosed inside the ice dome functioned as a thermal insulator and diminished the temperature and pressure gradients in the water and consequently suppressed the recirculation.

The simulation of the heat transfer in surrounding oil demonstrated that the average heat flux on the surface of smaller droplets is significantly larger than that on larger ones. This led to one of the essential findings observed in experiments and CFD that, when the droplet size doubles, the time required for the droplet to completely freeze extended by almost an order of magnitude. This finding can significantly contribute to applications involving emulsification, oil-water separation, and crystallisation processes.

Our immediate plans are to perform experiments with solid surfaces of different wettabilities to investigate the effect of contact angle on the freezing front propagation. We also plan to explore a similar arrangement in a crossflow (forced convection arrangement).

Acknowledgements

This work has been undertaken within the Consortium on Transient and Complex Multiphase Flows and Flow Assurance (TMF). In addition, the authors gratefully acknowledge the contributions made to this project by the following: - ASCOMP, BP Exploration; Cameron Technology & Development; CD-adapco; Chevron; KBC (FEESA); FORSYS; INTECSEA; Institutt for Energiteknikk (IFE); Kongsberg Oil & Gas Technologies; Wood Group Kenny; Petrobras; Schlumberger Information Solutions; Shell; SINTEF; Statoil and TOTAL. The authors wish to express their sincere gratitude for this support. The work was also supported by Russian Government "Megagrant" project 075-15-2019-1888, the UK Department for International Development (DFID) through the Royal Society-DFID Africa Capacity Building Initiative, and the UK Engineering and Physical Sciences Research Council (EPSRC) [grant numbers EP/K003976/1, EP/K008595/1, and EP/L020564/1]. The authors gratefully acknowledge the CHPC in the Republic of South Africa for providing the computing facilities and the software used the simulations. Data supporting this publication can be obtained on request from cep-lab@imperial.ac.uk.

References

[1] O. Fakorede, Z. Feger, H. Ibrahim, A. Ilinca, J. Perron, C. Masson, Ice protection systems for wind turbines in cold climate: characteristics, comparisons and analysis, Renew. Sustain. Energy Rev. 65 (2016) 662–675. https://doi.org/10.1016/j.rser.2016.06.080.

[2] S. Liu, H. Li, M. Song, B. Dai, Z. Sun, Impacts on the solidification of water on plate surface for cold energy storage using ice slurry, Appl. Energy. 227 (2018) 284–293. https://doi.org/10.1016/j.apenergy.2017.08.012.

[3] J. Wang, Z. Liu, Y. Gou, X. Zhang, S. Cheng, Deformation of freezing water droplets on a cold copper surface, Sci. China Ser. E Technol. Sci. 49 (2006) 590–600. https://doi.org/10.1007/s11431-006-2017-y.

[4] J.P. Hindmarsh, A.B. Russell, X.D. Chen, Experimental and numerical analysis of the temperature transition of a freezing food solution droplet, Chem. Eng. Sci. 59 (2004) 2503–2515. https://doi.org/10.1016/j.ces.2004.03.007.

[5] S. Tabakova, F. Feuillebois, S. Radev, Freezing of a supercooled spherical droplet with mixed boundary conditions, Proc. R. Soc. A Math. Phys. Eng. Sci. 466 (2010) 1117–1134. https://doi.org/10.1098/rspa.2009.0491.

[6] J.P. Hindmarsh, A.B. Russell, X.D. Chen, Experimental and numerical analysis of the temperature transition of a suspended freezing water droplet, Int. J. Heat Mass Transf. 46 (2003) 1199–1213. https://doi.org/10.1016/S0017-9310(02)00399-X.

[7] M. Strub, O. Jabbour, F. Strub, J.P. Bédécarrats, Experimental study and modelling of the crystallization of a water droplet, Int. J. Refrig. 26 (2003) 59–68. https://doi.org/10.1016/S0140-7007(02)00021-X.

[8] G. Chaudhary, R. Li, Freezing of water droplets on solid surfaces: An experimental and numerical study, Exp. Therm. Fluid Sci. 57 (2014) 86–93. https://doi.org/10.1016/j.expthermflusci.2014.04.007.

[9] A. Alizadeh, M. Yamada, R. Li, W. Shang, S. Otta, S. Zhong, L. Ge, A. Dhinojwala, K.R. Conway, V. Bahadur, A.J. Vinciquerra, B. Stephens, M.L. Blohm, Dynamics of ice nucleation on water repellent surfaces, Langmuir. 28 (2012) 3180–3186. https://doi.org/10.1021/la2045256.

[10] A.G. Mar ń, O.R. Enr úquez, P. Brunet, P. Colinet, J.H. Snoeijer, Universality of tip singularity formation in freezing water drops, Phys. Rev. Lett. 113 (2014) 054301. https://doi.org/10.1103/PhysRevLett.113.054301.

[11] V.N. Duy, T.V. Vu, A numerical study of a liquid drop solidifying on a vertical cold wall, Int. J. Heat Mass Transf. 127 (2018) 302–312. https://doi.org/10.1016/j.ijheatmasstransfer.2018.08.031.

[12] T.V. Vu, C.T. Nguyen, Q.H. Luu, Numerical study of a liquid drop on an inclined surface with solidification, Int. J. Heat Mass Transf. 144 (2019) 118636. https://doi.org/10.1016/j.ijheatmasstransfer.2019.118636.

[13] M.F. Ismail, P.R. Waghmare, Universality in freezing of an asymmetric drop, Appl. Phys. Lett. 109 (2016) 234105. https://doi.org/10.1063/1.4971995.

[14] O.R. Enr úquez, Á.G. Mar ń, K.G. Winkels, J.H. Snoeijer, Freezing singularities in water drops, Phys. Fluids. 24 (2012) 091102. https://doi.org/10.1063/1.4747185.

[15] J.H. Snoeijer, P. Brunet, Pointy ice-drops: How water freezes into a singular shape, Am. J. Phys. 80 (2012) 764–771. https://doi.org/10.1119/1.4726201.

[16] Z. Zhang, J. Gao, S. Zhang, Heat and mass transfer of the droplet vacuum freezing process based on the diffusion-controlled evaporation and phase transition mechanism, Sci. Rep. 6 (2016) 35324. https://doi.org/10.1038/srep35324.

[17] Y. Yao, R. Yang, C. Li, Z. Tao, H. Zhang, Investigation of the freezing process of water droplets based on average and local initial ice fraction, Exp. Heat Transf. 33 (2020) 197–209. https://doi.org/10.1080/08916152.2019.1600619.

[18] H. Sakaguchi, R. Ohmura, Y.H. Mori, Effects of kinetic inhibitors on the formation and growth of hydrate crystals at a liquid–liquid interface, J. Cryst. Growth. 247 (2003) 631–641. https://doi.org/10.1016/S0022-0248(02)02021-3.

[19] M. Cha, S. Baek, J. Morris, J.W. Lee, Hydrophobic particle effects on hydrate crystal growth at the water-oil interface, Chem. - An Asian J. 9 (2014) 261–267. https://doi.org/10.1002/asia.201300905.

[20] S. Jung, M.K. Tiwari, N.V. Doan, D. Poulikakos, Mechanism of supercooled droplet freezing on surfaces, Nat. Commun. 3 (2012) 615. https://doi.org/10.1038/ncomms1630.

[21] M. Song, C. Dang, T. Higashi, E. Hihara, Review of experimental data associated with the solidification characteristics of water droplets on a cold plate surface at the early frosting stage, Energy Build. 223 (2020) 110103. https://doi.org/10.1016/j.enbuild.2020.110103.

[22] Z. Jin, Q. Dong, S. Jin, Z. Yang, Visualization of the freezing and melting process of a small water droplet on a cold surface, in: Proc. Int. Conf. Fluid Dyn. Thermodyn. Technol. (FDTT 2012), Vol. 33, 2012.

[23] Z. Jin, S. Jin, Z. Yang, An experimental investigation into the icing and melting process of a water droplet impinging onto a superhydrophobic surface, Sci. China Physics, Mech. Astron. 56 (2013) 2047–2053. https://doi.org/10.1007/s11433-013-5209-z.

[24] D.M. Anderson, M.G. Worster, S.H. Davis, The case for a dynamic contact angle in containerless solidification, J. Cryst. Growth. 163 (1996) 329–338. https://doi.org/10.1016/0022-0248(95)00970-1.

[25] X. Zhang, X. Wu, J. Min, Freezing and melting of a sessile water droplet on a horizontal cold plate, Exp. Therm. Fluid Sci. 88 (2017) 1–7. https://doi.org/10.1016/j.expthermflusci.2017.05.009.

[26] X. Zhang, X. Liu, X. Wu, J. Min, Experimental investigation and statistical analysis of icing nucleation characteristics of sessile water droplets, Exp. Therm. Fluid Sci. 99 (2018) 26–34. https://doi.org/10.1016/j.expthermflusci.2018.07.027.

[27] Z. Liu, X. Zhang, H. Wang, S. Meng, S. Cheng, Influences of surface hydrophilicity on frost formation on a vertical cold plate under natural convection conditions, Exp. Therm. Fluid Sci. 31 (2007) 789–794. https://doi.org/10.1016/j.expthermflusci.2006.08.004.

[28] P. Hao, C. Lv, X. Zhang, Freezing of sessile water droplets on surfaces with various roughness and wettability, Appl. Phys. Lett. 104 (2014) 161609. https://doi.org/10.1063/1.4873345.

[29] S. Jung, M.K. Tiwari, D. Poulikakos, Frost halos from supercooled water droplets, Proc. Natl. Acad. Sci. 109 (2012) 16073–16078. https://doi.org/10.1073/pnas.1206121109.

[30] X. Zhang, X. Wu, J. Min, X. Liu, Modelling of sessile water droplet shape evolution during freezing with consideration of supercooling effect, Appl. Therm. Eng. 125 (2017) 644–651. https://doi.org/10.1016/j.applthermaleng.2017.07.017.

[31] X. Zhang, X. Liu, J. Min, X. Wu, Shape variation and unique tip formation of a sessile water droplet during freezing, Appl. Therm. Eng. 147 (2019) 927–934. https://doi.org/10.1016/j.applthermaleng.2018.09.040.

[32] M. Tembely, A. Dolatabadi, A comprehensive model for predicting droplet freezing features on a cold substrate, J. Fluid Mech. 859 (2019) 566–585. https://doi.org/10.1017/jfm.2018.839.

[33] A.R. Dehghani-Sanij, S. MacLachlan, G.F. Naterer, Y.S. Muzychka, R.D. Haynes, V. Enjilela, Multistage cooling and freezing of a saline spherical water droplet, Int. J. Therm. Sci. 147 (2020) 106095. https://doi.org/10.1016/j.ijthermalsci.2019.106095.

[34] A. Zadražil, F. Stepanek, O.K. Matar, Droplet spreading, imbibition and solidification on porous media, J. Fluid Mech. 562 (2006) 1. https://doi.org/10.1017/S0022112006000875.

[35] A. Virozub, I.G. Rasin, S. Brandon, Revisiting the constant growth angle: Estimation and verification via rigorous thermal modeling, J. Cryst. Growth. 310 (2008) 5416–5422. https://doi.org/10.1016/j.jcrysgro.2008.09.004.

[36] Y. Yao, C. Li, Z. Tao, R. Yang, Numerical simulation of water droplet freezing process on cold surface, in: Vol. 8 Heat Transf. Therm. Eng., American Society of Mechanical Engineers, 2017. https://doi.org/10.1115/IMECE2017-71175.

[37] V. S. Ajaev, S. H. Davis, The effect of tri-junction conditions in droplet solidification, J. Cryst. Growth. 264 (2004) 452–462. https://doi.org/10.1016/j.jcrysgro.2003.11.119.

[38] W.W. Schultz, M.G. Worster, D.M. Anderson, Solidifying sessile water droplets, in: Interact. Dyn. Convect. Solidif., Springer Netherlands, Dordrecht, 2001: pp. 209–226. https://doi.org/10.1007/978-94-015-9807-1_24.

[39] T. V. Vu, Deformation and breakup of a pendant drop with solidification, Int. J. Heat Mass Transf. 122 (2018) 341–353. https://doi.org/10.1016/j.ijheatmasstransfer.2018.01.125.

[40] T. Vu, C. Nguyen, D. Khanh, Direct numerical study of a molten metal drop solidifying on a cold plate with different wettability, Metals (Basel). 8 (2018) 47. https://doi.org/10.3390/met8010047.

[41] T. V. Vu, G. Tryggvason, S. Homma, J.C. Wells, Numerical investigations of drop solidification on a cold plate in the presence of volume change, Int. J. Multiph. Flow. 76 (2015) 73–85. https://doi.org/10.1016/j.ijmultiphaseflow.2015.07.005.

[42] T. V. Vu, G. Tryggvason, S. Homma, J.C. Wells, H. Takakura, A front-tracking method for three-phase computations of solidification with volume change, J. Chem. Eng. JAPAN. 46 (2013) 726–

731. https://doi.org/10.1252/jcej.13we169.

[43] X. Zhang, X. Liu, X. Wu, J. Min, Simulation and experiment on supercooled sessile water droplet freezing with special attention to supercooling and volume expansion effects, Int. J. Heat Mass Transf. 127 (2018) 975–985. https://doi.org/10.1016/j.ijheatmasstransfer.2018.07.021.

[44] H. Zhang, Y. Zhao, R. Lv, C. Yang, Freezing of sessile water droplet for various contact angles, Int. J. Therm. Sci. 101 (2016) 59–67. https://doi.org/10.1016/j.ijthermalsci.2015.10.027.

[45] T.V. Vu, K.V. Dao, B.D. Pham, Numerical simulation of the freezing process of a water drop attached to a cold plate, J. Mech. Sci. Technol. 32 (2018) 2119–2126. https://doi.org/10.1007/s12206-018-0421-4.

[46] T.V. Vu, J.C. Wells, Numerical simulations of solidification around two tandemly-arranged circular cylinders under forced convection, Int. J. Multiph. Flow. 89 (2017) 331–344. https://doi.org/10.1016/j.ijmultiphaseflow.2016.11.007.

[47] T.V. Vu, A.V. Truong, N.T.B. Hoang, D.K. Tran, Numerical investigations of solidification around a circular cylinder under forced convection, J. Mech. Sci. Technol. 30 (2016) 5019–5028. https://doi.org/10.1007/s12206-016-1021-9.

[48] T.V. Vu, Three-phase computation of solidification in an open horizontal circular cylinder, Int. J. Heat Mass Transf. 111 (2017) 398–409. https://doi.org/10.1016/j.ijheatmasstransfer.2017.04.011.

[49] T.V. Vu, Axisymmetric forced convection solidification of a liquid drop on a cold plate, Int. J. Multiph. Flow. 107 (2018) 104–115. https://doi.org/10.1016/j.ijmultiphaseflow.2018.05.023.

[50] T.V. Vu, Fully resolved simulations of drop solidification under forced convection, Int. J. Heat Mass Transf. 122 (2018) 252–263. https://doi.org/10.1016/j.ijheatmasstransfer.2018.01.124.

[51] W.D. Bennon, F.P. Incropera, A continuum model for momentum, heat and species transport in binary solid-liquid phase change systems—I. Model formulation, Int. J. Heat Mass Transf. 30 (1987) 2161–2170. https://doi.org/10.1016/0017-9310(87)90094-9.

[52] W.D. Bennon, F.P. Incropera, A continuum model for momentum, heat and species transport in binary solid-liquid phase change systems—II. Application to solidification in a rectangular cavity, Int. J. Heat Mass Transf. 30 (1987) 2171–2187. https://doi.org/10.1016/0017-9310(87)90095-0.

[53] V.R. Voller, M. Cross, N.C. Markatos, An enthalpy method for convection/diffusion phase change, Int. J. Numer. Methods Eng. 24 (1987) 271–284. https://doi.org/10.1002/nme.1620240119.

[54] A.D. Brent, V.R. Voller, K.J. Reid, Enthalpy-porosity technique for modeling convection-diffusion phase change: application to tthe melting of a pure metal, Numer. Heat Transf. 13 (1988) 297–318. https://doi.org/10.1080/10407788808913615.

[55] P.R. Chakraborty, Enthalpy porosity model for melting and solidification of pure-substances with large difference in phase specific heats, Int. Commun. Heat Mass Transf. 81 (2017) 183–189. https://doi.org/10.1016/j.icheatmasstransfer.2016.12.023.

[56] L. Karlsson, A.-L. Ljung, T.S. Lundstrom, Influence of internal natural convection on water droplets freezing on cold surfaces, in: Proceeding Proc. CONV-14 Int. Symp. Convect. Heat Mass Transf. June 8 - 13, 2014, Kusadasi, Turkey, Begellhouse, Connecticut, 2014: p. 8. https://doi.org/10.1615/ICHMT.2014.IntSympConvHeatMassTransf.110.

[57] L. Karlsson, A.-L. Ljung, T.S. Lundström, Modelling the dynamics of the flow within freezing water droplets, Heat Mass Transf. 54 (2018) 3761–3769. https://doi.org/10.1007/s00231-018-2396-1.

[58] A. Sciacchitano, D.R. Neal, B.L. Smith, S.O. Warner, P.P. Vlachos, B. Wieneke, F. Scarano, Collaborative framework for PIV uncertainty quantification: comparative assessment of methods,

Meas. Sci. Technol. 26 (2015) 074004. https://doi.org/10.1088/0957-0233/26/7/074004.

[59] V. Voulgaropoulos, N. Le Brun, A. Charogiannis, C.N. Markides, Transient freezing of water between two parallel plates: A combined experimental and modelling study, Int. J. Heat Mass Transf. 153 (2020) 119596. https://doi.org/10.1016/j.ijheatmasstransfer.2020.119596.

[60] F. Feuillebois, A. Lasek, P. Creismeas, F. Pigeonneau, A. Szaniawski, Freezing of a subcooled liquid droplet, J. Colloid Interface Sci. 169 (1995) 90–102. https://doi.org/10.1006/jcis.1995.1010.

[61] J. Blake, D. Thompson, D. Raps, T. Strobl, Simulating the freezing of supercooled water droplets impacting a cooled substrate, AIAA J. 53 (2015) 1725–1739. https://doi.org/10.2514/1.J053391.

[62] M.G. Worster, S.S.L. Peppin, J.S. Wettlaufer, Colloidal mushy layers, J. Fluid Mech. 914 (2021) A28. https://doi.org/10.1017/jfm.2020.863.

[63] M.R. Kadivar, M.A. Moghimi, P. Sapin, C.N. Markides, Annulus eccentricity optimisation of a phase-change material (PCM) horizontal double-pipe thermal energy store, J. Energy Storage. 26 (2019) 101030. https://doi.org/10.1016/j.est.2019.101030.

[64] H. Bazai, M.A. Moghimi, H.I. Mohammed, R. Babaei-Mahani, P. Talebizadehsardari, Numerical study of circular-elliptical double-pipe thermal energy storage systems, J. Energy Storage. 30 (2020) 101440. https://doi.org/10.1016/j.est.2020.101440.

[65] T.L. Bergman, A.S. Lavine, F.P. Incropera, D.P. DeWitt, Introduction to heat transfer, 6th ed., John Wiley & Sons, Inc., 2011.

[66] ANSYS Fluent theory guide, (2018).

[67] S. Wildeman, S. Sterl, C. Sun, D. Lohse, Fast dynamics of water droplets freezing from the outside in, Phys. Rev. Lett. 118 (2017) 084101. https://doi.org/10.1103/PhysRevLett.118.084101.

[68] I. V. Roisman, C. Tropea, Wetting and icing of surfaces, Curr. Opin. Colloid Interface Sci. 53 (2020) 101400. https://doi.org/10.1016/j.cocis.2020.101400.